



PERGAMON

International Journal of Impact Engineering 22 (1999) 855–886

INTERNATIONAL
JOURNAL OF
IMPACT
ENGINEERING

www.elsevier.com/locate/ijimpeng

Ballistic penetration of steel plates

T. Børvik^{a,*}, M. Langseth^b, O.S. Hopperstad^b, K.A. Malo^b

^a*Norwegian Defence Construction Service, Central Staff/Technical Division, N-0015 Oslo, Norway*

^b*Department of Structural Engineering, Norwegian University of Science and Technology, N-7034 Trondheim, Norway*

Received 23 October 1998; received in revised form 3 February 1999

Abstract

This paper presents a research programme in progress where the main objective is to study the behaviour of Weldox 460 E steel plates impacted by blunt-nosed cylindrical projectiles in the lower ordnance velocity regime. A compressed gas gun is used to carry out high-precision tests, and a digital high-speed camera system is used to photograph the penetration process. A coupled constitutive model of viscoplasticity and ductile damage is formulated and implemented into the non-linear finite element code LS-DYNA, and the material constants for the target plate are determined. The proposed model is applied in simulations of the plate penetration problem and the results are compared with test data. Good agreement between the numerical simulations and the experimental results is found for velocities well above the ballistic limit, while the ballistic limit itself is overestimated by approximately 10% in the numerical simulations. © 1999 Elsevier Science Ltd. All rights reserved.

Keywords: Ballistic penetration; Experimental tests; Viscoplasticity; Damage; Numerical simulations

1. Introduction

Impact and impact related problems have been a considerable research topic for decades, and substantial effort has been invested in order to physically understand and mathematically describe the phenomena taking place during ordnance ballistic penetration [1–7]. So far, most progress has been made during experimental investigations of the normal perforation of metal plates, and a large number of studies can be found in the literature [8–15]. However, due to the complexity and costs related to ballistic experiments it is not optimal to base all impact related studies on laboratory tests alone. Therefore, a general solution technique is requested as a supplement to high-precision testing in order to reduce the experimental needs to a minimum.

* Corresponding author. Tel.: + 47-73-59-46-47; fax: + 47-73-59-45-35.

E-mail address: tore.borvik@bygg.ntnu.no (T. Børvik)

A number of analytical models have been proposed over the years [16–23], but the complexity of many impact events often limits the general use of closed-form analytical solutions. It may therefore be preferable to use numerical methods in the attempt to solve this class of problems. However, numerical studies involving impact and penetration in the sub-ordnance and ordnance velocity regime are still few in the literature, even though the finite element method has been adopted as a general tool in most communities. The reason may be that the method does not have the accuracy and robustness required for reliable material description and fracture calculation during perforation [28]. Earlier work using, e.g., erosion techniques and element-kill options [24] has revealed some weaknesses [25–27], and according to Belytschko [28] finite element simulations including geometrical and material instabilities, combined with discontinuities in space and time, are still very difficult to treat computationally. Thus, special attention is needed to make progress.

This paper is based on a research programme in progress where the main objective is to study the behaviour of steel plates impacted by blunt-nosed projectiles. In order to make progress, substantial knowledge regarding the physical phenomena controlling the penetration problem is necessary. Such information is obtained through high-precision penetration tests and material tests under impact generated high strain-rate loading conditions. The experimental findings are used to validate if a computational model of viscoplasticity and ductile damage can be used to numerically predict the target response during penetration.

In the paper, some of the experimental and numerical work carried out so far will be summarised, compared and discussed. Finally, some preliminary conclusions from the project are given.

2. Experimental set-up

The compressed gas gun shown in Fig. 1 [29] has been designed in order to launch the projectile. The main components of the gas gun are the 200 bar pressure tank, the purpose-built firing section for compressed gas, the 10 m long smooth barrel of calibre 50 mm and the closed 16 m³ impact chamber. The gas gun is capable of launching a 250 g projectile package to a maximum velocity of 1000 m/s when helium is used as a propellant gas. The projectile is mounted in an 8-pieced serrated sabot with an obturator and inserted into the rear section of the barrel. To reduce the sabot weight, which is known to be crucial regarding sabot separation and subsequent pitch and yaw, the sabot is manufactured from a combination of polycarbonat and foam. When the sabot package leaves the muzzle, the sabot is immediately separated from the projectile due to aerodynamic forces. A sabot trap, located about 1.5 m from the muzzle, allows the projectile to pass freely while the sabot parts are stopped. The projectile then passes the initial velocity measurement station before it impacts the target after about 2 m of free flight. The target is clamped in a circular frame, having an inner clamp diameter of 500 mm. To allow high-speed photography during impact, the clamping system is equipped with a 150 mm framing window. If the projectile perforates the target, residual velocities are measured before all free flying objects are stopped without further damage in a rag-box. After testing, the impact chamber is opened for final inspections and measurements of the target, projectile and plug.

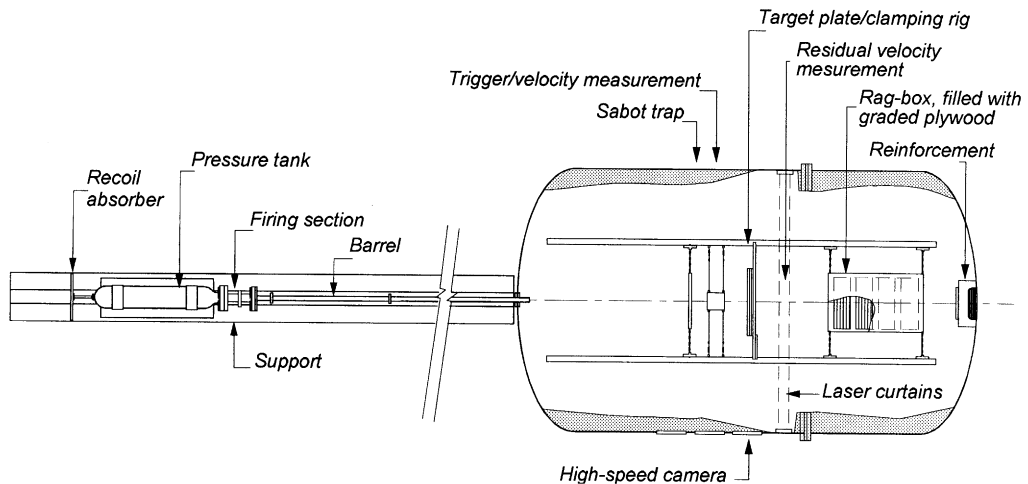


Fig. 1. Sketch of compressed gas gun [29].

To measure initial projectile velocity (v_i), a photocell system having two identical light-barriers with LED-light sources on the upper side of the projectile path and detectors on the lower side has been constructed. When the projectile passes between the sources and detectors in the light-barrier, light is interrupted and signals are given to a nanosecond counter. The second light-barrier also works as a trigger for the digital high-speed camera system. A similar system was developed to measure residual velocities (v_r) if perforation takes place. Here, each light source consists of six lasers mounted in line to give parallel beams. Detectors are mounted in two lines to match the laser light sources. The detectors feed an amplifier followed by a trigger that detects any abrupt decrease in signal level. When the output signals are stored on a digital oscilloscope, information regarding velocity and length of all passing objects is obtained. The accuracy of the systems is proven to be high [29].

It is important to be able to observe the different events during ballistic penetration. However, until recently photographic techniques in particular have been limited by time-consuming film development or moderate framing rates during testing. These obstacles have been overcome by camera systems that combine the advantages of an image converter camera and a CCD camera. The image converter camera provides extremely fast shutter speeds, while the CCD camera provides digital images that are available immediately after the experiment. In this study the Ultracac FS 501 digital high-speed image converter camera [30,31] is used both for visualisation and measurements of the penetration process. The system is fully computer operated and capable of framing rates from 2000 to 20,000,000 frames per second with exposure times down to 10 ns. In framing mode each exposure and interframe time can be independently selected, and the image format may be chosen from 8 to 24 pictures. The CCD readout system uses a high-resolution chip of 2048×2048 pixels with 16 bit dynamic resolution. The camera system is set perpendicular to the projectile path in the target plane in order to record the projectile both before and after perforation. To reconstruct a full 3D description of the penetration process, mirrors are mounted above the

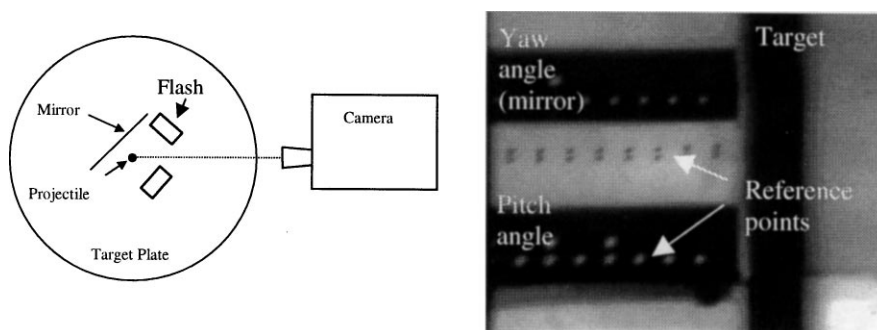


Fig. 2. Set-up of high-speed camera system giving 3D images [30].

projectile path at an angle of 45° with respect to the centreline of the camera, one on each side of the target plate (see Fig. 2). However, both the aligning of the system and the luminance during testing are crucial parameters in order to have good, reliable images. In this study, 4 flash heads of 60 J and 2 flash heads of 550 J have been used to get sufficient lighting.

As indicated above, the high-speed camera system is also used for measurements. This is made possible by advanced image processing of the digital pictures, and several computer sub-routines have been developed [31]. The most important feature is the possibility to obtain travelled distance, velocity and acceleration as a function of penetration time for the assumed rigid bodies. This is illustrated in Fig. 3. Both the moving projectile and the stationary support are equipped with fiducial marks, which typically are white dots giving maximum contrast in the image. Each dot is identified by the cursor, and the sub-routine calculates the centre of gravity of the fiducial mark based on the intensity of the pixels within the defined area. Thus, the co-ordinates of the fiducial mark are determined. This is done for several fiducial marks both on the moving body and the stationary support. Moving to the next image, the relative distance moved by the body is found if the same fiducial marks as in the previous image are detected. The time step Δt between the images is known and set by the user prior to the test. By making use of a known calibration value that transforms pixels into millimetres, the average velocity and acceleration can be calculated. The procedure is repeated for all images within the full frame, and the velocity–time curve is constructed. Due to the sub-pixel resolution, gained by calculating the centre of gravity for each fiducial mark, the accuracy of the velocity measurements is generally high. Also angles can be measured as a function of penetration time [30,31], and a comprehensive high-speed camera calibration routine has been developed in order to correct aberrations known to appear in the digital images [31].

3. Experimental results

The main objective of the experimental investigations performed in this project is to study the different phenomena taking place during ballistic penetration. At the same time, high-precision test data becomes available for validation of solution methods. In this particular paper, emphasis will be on an experimental programme carried out to determine the ballistic limit curve of a 12 mm

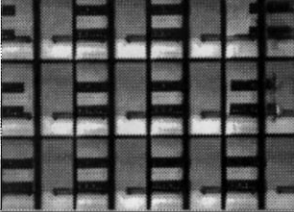
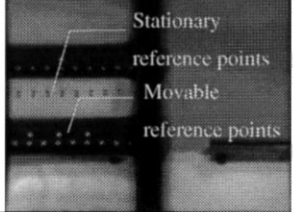
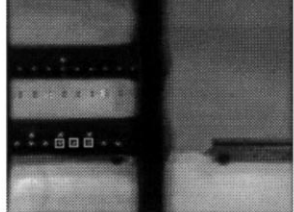
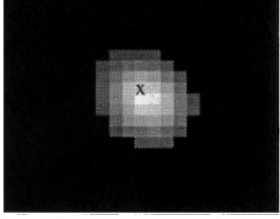
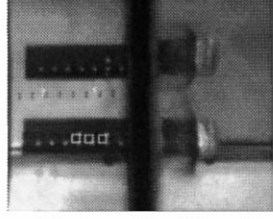
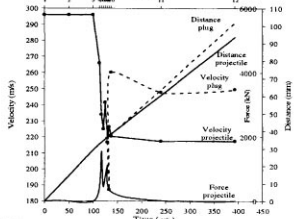
1. Full frame	2. Image	3. Selection of fiducial marks
		
<p>The full frame picture of the test is shown. The total number of points to measure is selected.</p>	<p>The different images within the full frame are selected and enlarged, one by one.</p>	<p>Fiducial marks on the projectile and support are marked by the cursor, and detected by the program.</p>
4. Centre of gravity	5. Repetition of procedure	6. Results
		
<p>The point is enlarged 10 times. Unwanted pixels are removed, and the centre of gravity is calculated based on the pixel intensity.</p>	<p>The procedure is repeated for all images in the test. The sub-pixel distance moved between each image is calculated.</p>	<p>Based on the known time interval and a calibration value, distance, velocity and acceleration are found as a function of time.</p>

Fig. 3. Procedure for calculation of velocity as a function of time [31].

thick Weldox 460 E steel plate. Data and observations from a similar experimental programme on a 10 mm thick Weldox 460 E steel plate [32] are in addition given for comparison.

Blunt-nosed cylindrical projectiles are machined from Arne tool steel, having a nominal mass (m_p), diameter (d_p) and length (l_p) of 197 g, 20 mm and 80 mm, respectively. The total mass of the sabot is in addition approximately 90 g for all tests. After machining, the projectiles are oil-hardened to a nominal Rockwell C value of 53 ($\sigma_0 \approx 1850$ MPa). Even if this represents an upper limit for projectile hardness, plastic deformation may appear in the nose part. Finally, the projectiles are painted dead black, measured and equipped with fiducial marks. All targets are manufactured from the same Weldox 460 E steel plate, having a nominal plate thickness (h_p) of 12 mm and material properties as given in Table 2. After careful cutting from the larger plate and sandblasting on both sides, 21 equally spaced holes are drilled on a 550 mm diameter bolt circle and the target is clamped in a rigid frame with an inner clamp diameter of 500 mm. Finally, geometrical imperfections, thickness and initial oblique are measured.

The experimental programme and some important test results are given in Table 1, while Fig. 4 shows a graphical representation of the most interesting response parameters obtained during testing. All parameters are kept constant in the tests except for the impact velocity (v_i), which are

Table 1
Experimental results of 12 mm thick Weldox 460 E steel plates

Test #	v_i (m/s)	v_r (m/s)	v_{rpl} (m/s)	m_p (g)	m_{pl} (g)	h_t (mm)	w_{max} (mm)	θ_f (mm)	θ_r (mm)
1	303.5	199.7	242.3	196.6	27.6	12.1	1.01	20.65	20.93
2	244.2	132.6	187.7	196.9	28.1	12.1	1.22	20.42	21.18
3	285.4	181.1	224.7	197.3	27.6	12.0	1.22	20.59	20.75
4	200.4	71.4	103.7	197.0	27.8	12.0	2.08	20.35	20.88
5	199.1	67.3	104.0	196.9	27.8	12.1	1.92	20.28	20.65
6	188.8	43.2	66.9	196.9	27.8	12.0	2.32	20.36	20.68
7	173.7	0	0	196.1	–	12.1	2.93	20.19	–
8	181.5	0	0	196.7	–	12.1	2.92	20.21	–
9	224.7	113.7	169.0	196.9	27.3	12.0	–	20.56	20.72
10	179.4	0	0	196.8	–	12.0	2.81	20.14	–
11	189.6	43.7	71.8	196.9	27.9	12.1	1.98	20.40	20.77
12	189.2	40.1	66.8	196.7	28.0	12.1	1.87	20.36	20.63
13	177.3	0	0	197.0	–	12.1	2.95	20.21	–
14	184.3	30.8	45.3	196.8	27.8	12.1	2.04	20.35	20.64
15	189.6	42.0	64.0	196.7	27.7	12.1	2.06	20.34	20.63
16	184.8	0	0	196.9	–	12.1	2.59	20.20	–

varied between 170 and 310 m/s, representing velocities just below and well above the ballistic limit velocity (v_{bl}) of the target material.

Pitch and yaw angles are measured from the digital high-speed camera images just prior to impact in order to determine the projectile's path during free flight [31]. From all tests, the total yaw angle at impact is found to be small and normally between 0.5 and 1°. These values are well below the critical value of 3–4°, known to give an increase in the ballistic limit velocity as reported in e.g. [4,33]. Also target oblique is measured and found negligible.

The ballistic limit curve for the 12 mm thick Weldox 460 E steel plate shown in Fig. 4a is constructed based on the measured initial (v_i) and residual (v_r) projectile velocities given in Table 1. Several tests are performed in an attempt to determine the ballistic limit velocity as closely as possible, and the difference between the highest velocity not giving perforation (test # 12-16) and the lowest velocity giving complete perforation (test # 12-14) is found to be less than 0.5 m/s. The residual velocity of the plug (v_{rpl}), which is plotted in Fig. 4a for comparison, is always found to be higher than that of the projectile even if the velocities seem to be similar immediately after fracture. This sudden increase in plug velocity after fracture is assumed caused by stress waves in the projectile and plug. The ratio between the velocity curves is found to decrease with increasing velocity.

From the plotted data it is not clear if a distinct jump as indicated in [34] is present in these experiments. A small jump at the ballistic limit seems to appear, but this may be due to scatter in the target material properties. However, it has been noticed that the target material is sensitive to variations in velocity near the ballistic limit, and that the residual velocity of the projectile is never small.

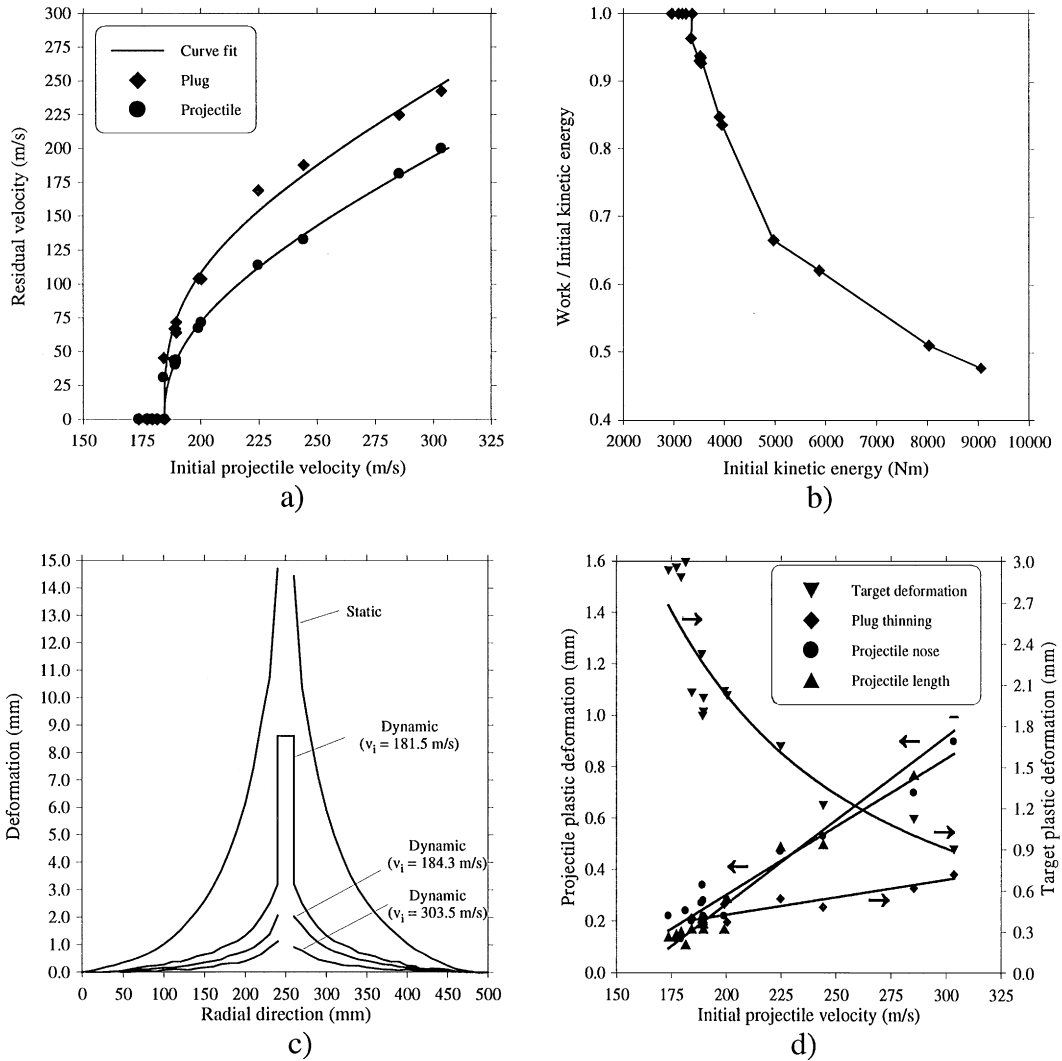


Fig. 4. Graphical representation of important response parameters.

The experimental data has been fitted to a model proposed by Lambert [4] in order to calculate residual projectile velocity (v_r) as a function of the measured initial projectile velocity (v_i) and the experimentally obtained ballistic limit velocity (v_{bl})

$$v_r = \begin{cases} 0 & 0 \leq v_i \leq v_{bl}, \\ a(v_i^p - v_{bl}^p)^{1/p} & v_i > v_{bl}. \end{cases} \quad (1)$$

By using the method of least squares the model constants a and p are found to be 0.76 and 2.36, respectively, and as seen from Fig. 4a excellent agreement between the experimental data and the model fit is obtained. If p is chosen equal to 2, a curve fit gives a equal to 0.85. These values of a and p lead us to the model proposed by Recht and Ipson [35], where conservation of energy and momentum is used to determine an expression for residual projectile velocity. In the Recht–Ipson model, p is equal to 2 and a is given as a mass ratio:

$$a = \frac{m_p}{m_p + m_{pl}}, \quad m_{pl} \approx \pi r_p^2 \rho_t h_t. \quad (2)$$

Under the conditions described in this programme the mass ratio a becomes 0.87, which is close to the fitted value. A comparison between the experimental data and the Recht–Ipson model is shown in Fig. 18. Another observation is that the ballistic limit velocity can be found from only a few experimental tests using Eq. (1), when v_{bl} is taken as the unknown. If, e.g. test # 12-9 in Table 1 is selected, the ballistic limit velocity is calculated to be 182.8 m/s, which is close to the measured ballistic limit of 184.5 m/s. Even if the accuracy of the method is questionable in other situations, it shows that simple energy balances can give reasonable estimates of the overall target response.

Projectile kinetic energy is transformed into target and projectile work through a complex stress wave transfer at impact, and it is difficult to quantitatively address the energy dissipation during penetration. However, the total amount of energy absorbed may easily be calculated using conservation of energy. This is indicated in Fig. 4b, where the amount of initial kinetic energy converted into work is plotted as a function of initial kinetic energy. As seen, the percentage of work carried out by the system decreases with increasing impact velocity. At the highest projectile velocities the energy absorption seems to flatten out, indicating that no more energy can be absorbed by the projectile–target system. At the ballistic limit, the total amount of energy absorbed during impact is found to be 35% less than the amount of energy absorbed under similar quasi-static plugging conditions [36].

The target deformation consists of a combination of localised bulging and global dishing, and the importance of impact velocity is demonstrated in Fig. 4c. In the case of static loading [36], the plastic deformation reaches out to the boundary and energy is absorbed as membrane stretching. In the dynamic case, the deformation is much more localised. The permanent target deformation, measured after the test, increases with increasing velocity until it reaches a maximum at the ballistic limit. The maximum deformation (w_{max}) is less than half the plate thickness, indicating that the global response during impact is dominated by bending stresses. After perforation, the deformation decreases with velocity until it stabilises at a velocity well above the ballistic limit. However, the maximum deformation during penetration is observed to be higher. Both from the static and dynamic tests evidence is found that the maximum deformation close to fracture is about twice as large as the permanent deformation, indicating a considerable elastic rebound in the target. Although the permanent deformation is found to be small, global target deformation dissipates a considerable amount of the initial kinetic energy during impact. Some typical cross-sections of penetrated target plates at increasing initial projectile velocity are shown in Fig. 5.

Fig. 4d shows measured geometrical values as a function of initial projectile velocity. The permanent target deformation decreases from a maximum value at the ballistic limit towards a constant value at higher projectile velocities, as also indicated in Fig. 4c. The plug thinning due to

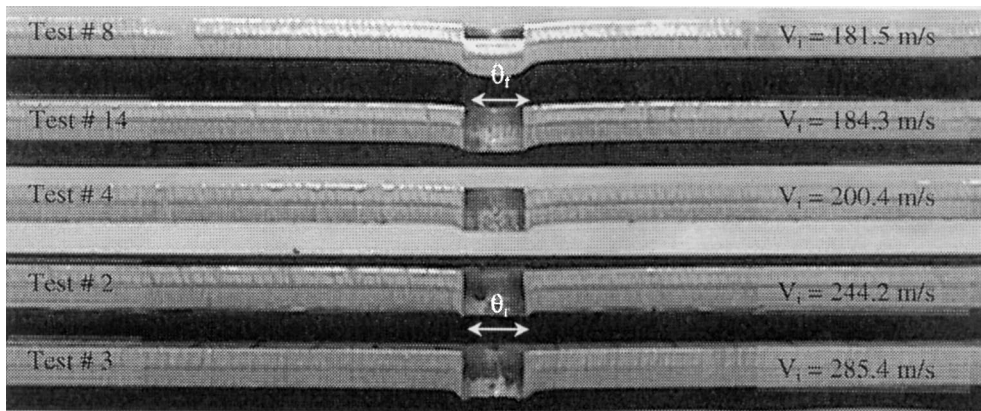


Fig. 5. Cross-sections of penetrated 12 mm thick Weldox 460 E steel targets.

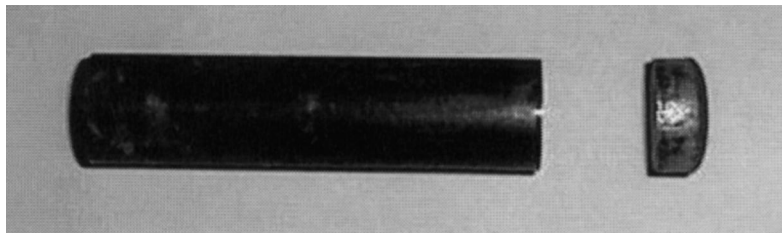


Fig. 6. Typical projectile and plug after perforation.

compression, defined as the difference between the initial target thickness and the final plug thickness, is seen to increase slightly with increasing projectile velocity. However, the plug mass (m_{pl}) is almost constant for all velocities. This is caused by an increase in plug diameter with velocity due to projectile mushrooming, which takes place during the first stage of penetration. The diameter of the front side of the plug is equal to the final diameter of the projectile and always larger than the target cavity diameter (θ_f). The rear side diameter of the plug and target cavity (θ_r) is somewhat larger due to tensile stretching. Even if maximum hardened, the projectile is plastically deformed at impact. Above this hardness limit, the projectile will fracture. During deformation, the projectile length is decreased and the projectile nose diameter is increased as a function of velocity. Furthermore, it seems that there exists a threshold velocity for projectile deformation. Above this velocity considerable mushrooming in the projectile starts to appear. By making post-impact measurements of the deformed shape [37], it is possible to estimate the amount of energy absorbed in the projectile during impact. At the highest velocities used in this study, as much as 10–15% of the total energy is assumed dissipated in projectile plastic deformation.

Finally, the Rockwell C (HRC) hardness of the projectile is measured both before and after impact. It is always found that the hardness is reduced by 2–3 HRC during penetration. This indicates damage in the nose part as a result of the impact. Fig. 6 shows a typical projectile and plug after perforation.

The indentation of the projectile gives rise to a relative velocity within the target, and the global deformation mode changes into a mechanism of highly localised shear around the projectile nose. The width of the shear zone is a function of the relative velocity, and may turn into an intense shear band if the velocity becomes sufficiently high. The shear failure is isothermal, adiabatic or in the transition stage from isothermal to fully adiabatic depending on the rate of loading. According to Lindholm [38], the failure in steel will be adiabatic if the strain-rate exceeds 100 s^{-1} . From the high-speed camera measurements, evidence is found that the perforation time is less than $100 \mu\text{s}$, except for the tests very close to the ballistic limit. This indicates that the strain rate in the shear zone has been much higher than 100 s^{-1} , and that the process can be considered as adiabatic. In an adiabatic process, where the conduction of heat generated by the plastic deformation is negligible, strain-hardening effects may be overcome by thermal softening, giving a thermal instability.

In order to investigate the possible influence of thermal effects and the local stress state in the target during penetration, a micromechanical investigation is in progress [39]. So far, only 10 mm thick targets have been investigated. Sign of temperature effects has been investigated using a scanning electron microscope. No proof of appreciable adiabatic overheating, visible as molten material, intensive white shear bands, recrystallisation or recovery, has been found in the shear zone. This indicates that the temperature in the material has not exceeded 400°C . By assuming adiabatic conditions, the temperature rise in the target caused by conversion of plastic work into heat can be calculated as [38]

$$\Delta T = \frac{\alpha}{\rho C_p} \int_0^{\gamma_c} \tau \, d\gamma \quad (3)$$

where α is the proportionality constant, ρ is the density and C_p is the specific heat (see Table 2). This equation gives a temperature rise in the target material during impact of $300\text{--}350^\circ\text{C}$. From the numerical simulations in Section 5, where the energy dissipation is calculated and converted into heat, approximately the same result is obtained. A clear blue colour, characteristic for the blue brittle region described in Section 4, is clearly seen on the fracture surface of the targets. In Fig. 11d, the blue brittle region appears at a temperature of about 300°C . All this experimental evidence indicates that the temperature rise in the target under the conditions described in this study is about $300\text{--}350^\circ\text{C}$.

The stress state in the target and the mode of failure during perforation has also been investigated in the microscope. Fig. 7 shows the cross-section of a 10 mm thick target at the ballistic limit [39], and several important observations are found. First of all, the dark lines of pearlite running parallel to the plate surface as a result of the manufacturing process show that there are at least three different stress states in the target during perforation. The first stage, where the flow lines are hardly distorted, is due to compression. This stage is rapidly overcome when the plug is set in motion by the moving projectile and the deformation mechanism changes into a localised shear zone throughout the target thickness. As seen in Fig. 7, the width of the intense shear zone is rather constant. When the plug has moved approximately half a plate thickness, fracture occurs. This final stage includes a combination of shear and tensile stresses. It is also seen that the fracture starts at the projectile–plug interface and propagates towards the rear surface. Finally, note that when the plug is completely free on one side, cracking has just started on

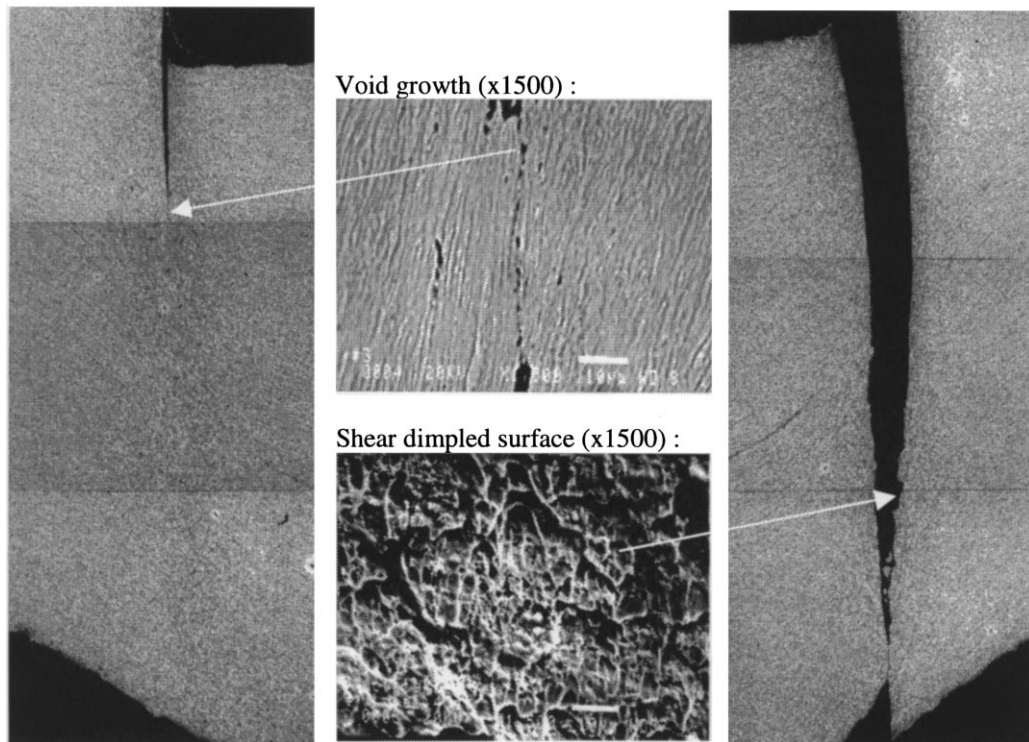
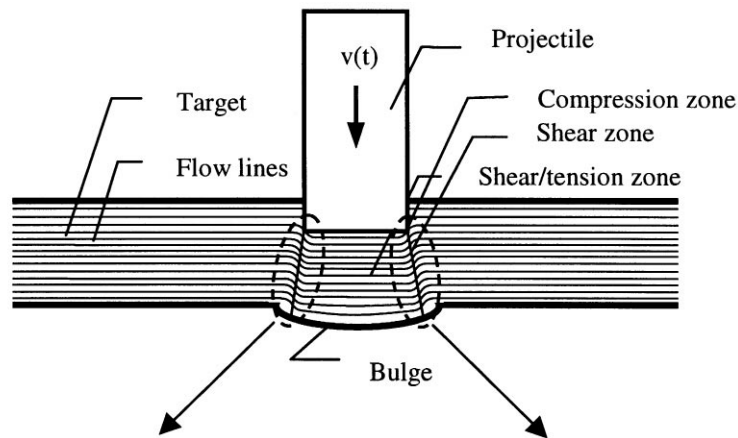


Fig. 7. Metallurgical images of the localised shear zone ($\times 32$). Note that the pictures showing the shear zones are constructed based on several images.

the other side. This unsymmetrical fracture mode is responsible for the observed plug rotation after complete separation.

The fracture surfaces and the different fracture morphology regions have been studied in detail in the scanning electron microscope. Two typical images from this study are also presented in Fig. 7.

From the front face to the rear side of the target one can see a sharp edge of the indentation without any frontal bulge, followed by a shear region smoothed by the passing projectile. Towards the rear side, a region of shear dimples appears. In the concentrated shear zone, voids are initiated. Due to the continuous straining, the voids grow and elongate. The voids then coalesce due to fracture of the thin walls separating the voids, giving the obtained dimples, and the crack is allowed to grow. This type of behaviour denotes ductile fracture [40]. Of even more interest, the area in front of the crack tip has been investigated. A number of elliptical cavities are found along the localised shear zone, showing how the voids nucleate, grow and coalesce in front of the crack to form the ductile fracture. This observation justifies the assumption of using continuum damage mechanics in order to describe the ductile fracture, as presented in Section 4.

Two typical perforation tests are selected for a more detailed study. The results from these tests will be compared to the numerical simulations given in Section 5. High-speed camera images from the tests are shown in Figs. 8 and 9. In Fig. 8 a 10 mm thick Weldox 460 E steel plate is perforated by a projectile with an initial velocity of 296 m/s, which is well above the ballistic limit (test # 10-9 in [32]). In Fig. 9, a 12 mm thick Weldox 460 E steel plate is perforated by a projectile having an initial velocity of 189.6 m/s, which is close to the ballistic limit (test # 15 in Table 1). In Fig. 8 mirrors are used to give a 3D description of the penetration process (see Fig. 2) and the camera is operating in a 12 image mode. No mirrors are used in Fig. 9, and a 15 image mode is used. In the latter, the stationary reference points are seen in the lower-left corner of the different images.

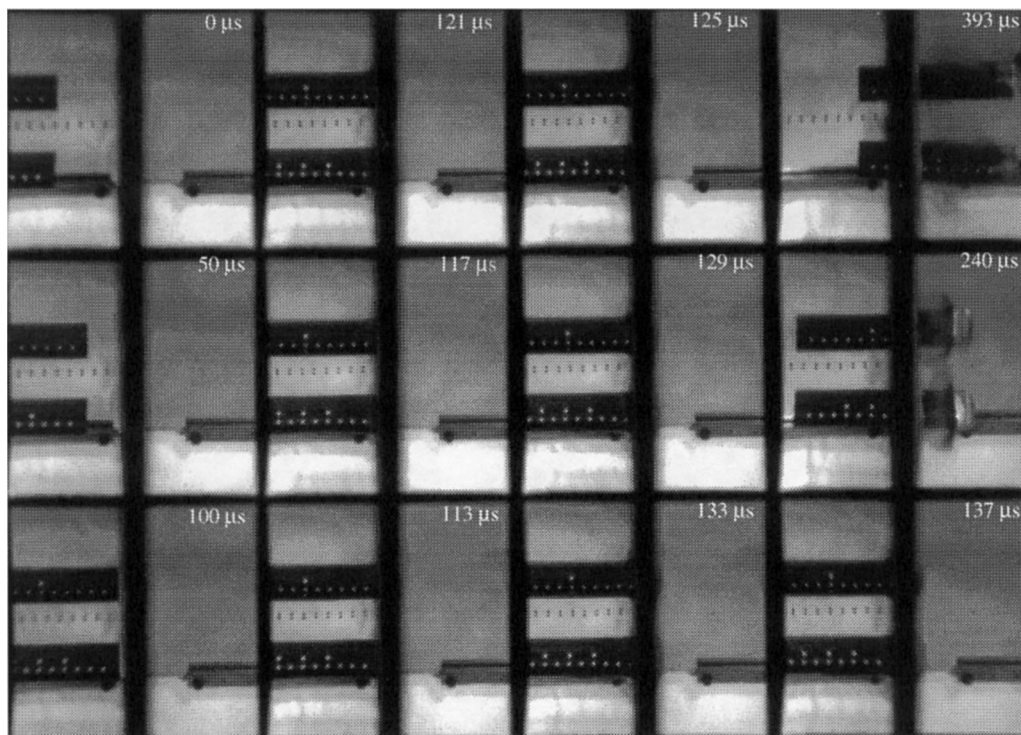


Fig. 8. Perforation of 10 mm thick Weldox 460 E steel plate (test # 10-9 in [32]).

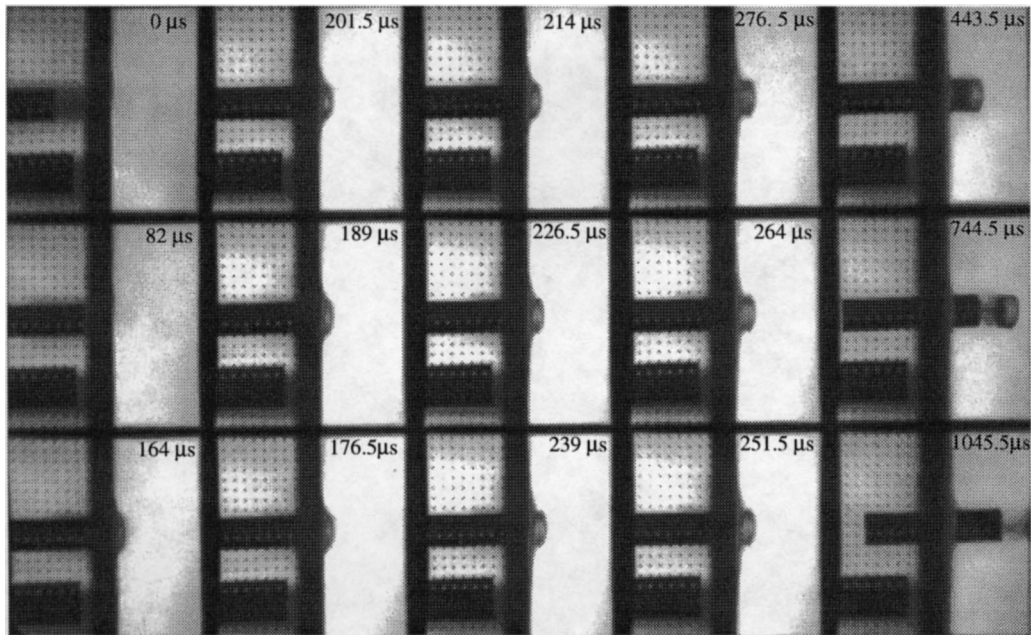


Fig. 9. Perforation of 12 mm thick Weldox 460 E steel plate (test # 12-15).

From these and similar pictures some immediate conclusions can be drawn. The projectile is embedded in the target before any considerable bulging of the rear side appears (Fig. 8), justifying the assumption of a stationary compression stage. The bulge is highly localised, showing hardly any radial distribution before fracture. This is valid for most tests, except for those closest to the ballistic limit where perforation is a much slower process and a larger part of the target plate is activated (Fig. 9). Furthermore, the plug fractures when the projectile has indented approximately half the target thickness. It is then pushed out of the cavity by the projectile before complete separation occurs. In most cases, the projectile and plug have identical velocities immediately after perforation. Afterwards they separate and the plug leaves the projectile at a higher velocity. Some of the images have revealed considerable plug rotation after complete separation due to the unsymmetrical fracture mode seen in Fig. 7. No significant angle deviation of the projectile after perforation is found.

The digital high-speed camera images are also used for direct measurements of travelled distance as a function of penetration time [31]. This is used to calculate projectile and plug velocity and acceleration during testing. The average velocity is defined as a vector quantity equal to the moved distance of the projectile divided by the known time interval. The average acceleration is given as the vector change in velocity divided by the time interval. The high-speed camera measurements are shown in Fig. 10. As seen from Fig. 10a, the projectile in test # 10-9 (Fig. 8) impacts the target after about 100 μs at a velocity of 296 m/s. During the next ~ 40 μs the projectile indents the target, giving a sharp velocity drop, and it perforates at a velocity of 218 m/s. However, it is hard to determine the point of impact and the perforation time exactly since the camera system provides

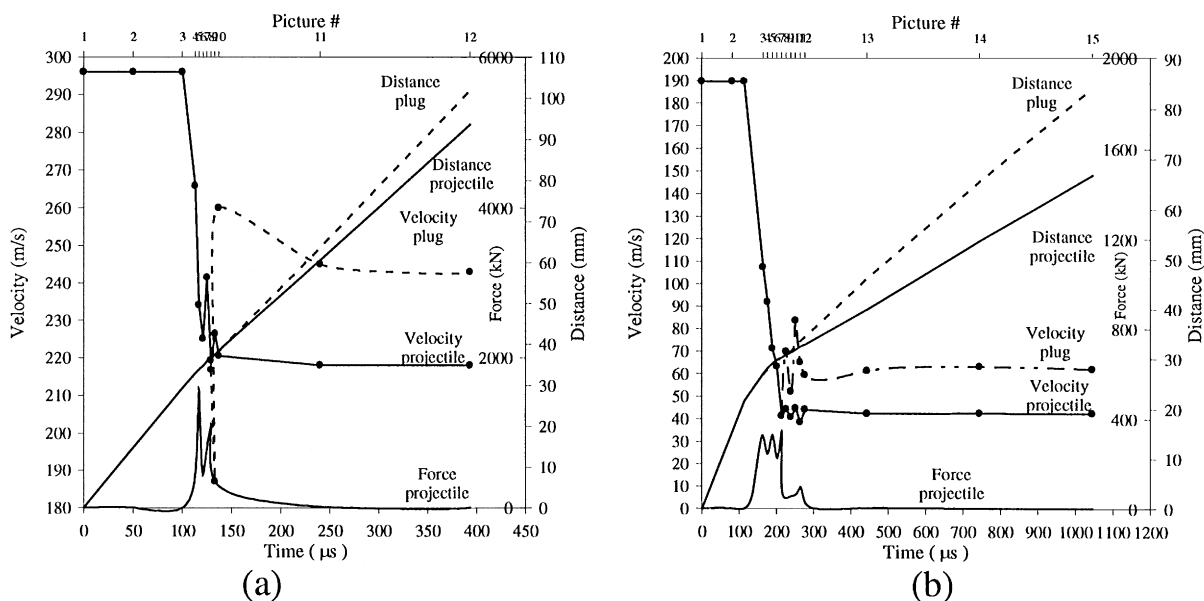


Fig. 10. High-speed camera measurements of (a) test # 10-9 and (b) test # 12-15.

only a limited number of images. In test # 10-9 the point of impact seems to be missed by some microseconds, since the final slope of the measured velocity–time curve is steeper than the initial slope. The velocity after perforation is almost constant, indicating a negligible sliding friction between the projectile and target after fracture. However, the possible influence of sliding and sticking friction during penetration is still unknown. The plug shows a rapid velocity increase before it stabilises at a velocity approximately 15% higher than that of the projectile. A similar behaviour is obtained in Fig. 10b for the penetration process in test # 12-15. In this test the camera missed the point of impact due to an inaccurate trigger. However, since the distance from the trigger to the target is known for all these tests, the measured velocity–time curve was corrected according to the assumed point of impact. This gives that the projectile impacts the target after about $114 \mu\text{s}$ at a velocity of 189.6 m/s . During the next $100 \mu\text{s}$ the projectile perforates the target, having a residual velocity of 42 m/s . As seen, the process is much slower near the ballistic limit. In this test the residual velocity of the plug is found to be 50% higher than that of the projectile. Finally, the average force on the projectile seems to be considerable higher in Fig. 10a due to a steeper velocity drop. The force calculations are believed to be rather inaccurate since they are based on the measured acceleration from a limited number of images.

The velocities calculated using the high-speed camera images are in close agreement (within 1–2%) with those obtained by the photocell system described in Section 2. However, the measured velocity–time curves show some peaks near the fracture region. This may be due to aberrations in the digital images, or it could as well be caused by a physical effect due to several impacts between the projectile and plug during penetration. The numerical simulations have revealed such impacts

between the projectile and plug, but this is for the time being not clear and further investigations are necessary.

4. Material behaviour and modelling

To be able to describe the various phenomena taking place during ballistic penetration, it is necessary to characterise the behaviour of materials under impact-generated high strain rate loading conditions. The characterisation involves not only the stress–strain response at large strains, different strain rates and temperatures, but also the accumulation of damage and the mode of failure. Such complex material behaviour involving fracture is difficult to describe in analytical models. In numerical simulations, constitutive models of nearly any degree of complexity can be incorporated into the code. However, due to the many difficulties in obtaining model constants for dynamic material behaviour, engineering models may be preferable to more sophisticated models [5]. Another important feature is the physical difference between plastic flow and fracture. In ductile metals, plastic flow may be viewed macroscopically as a visible shape change, microscopically as the appearance of slip lines, and at the atomic level as the movement of dislocations. It is also known that plastic flow is driven by the deviatoric stress state in the material. Initiation of damage is due to arrests of dislocations by microdefects or microstress concentrations giving decohesion and subsequently nucleation, growth and coalescence of microcracks and microvoids [41]. The damage evolution is strongly influenced by the hydrostatic stress state in the material [42,43]. Accordingly, different mathematical models are needed to describe plastic flow and fracture.

In this paper numerical simulations are carried out and compared with experimental data using a coupled material model of viscoplasticity and ductile damage, developed for impact and penetration problems. Here, only the main features of the model will be given, while the details in the formulation are presented by Hopperstad et al. [44]. The model is formulated within the framework of viscoplasticity and continuum damage mechanics [42], allowing for large plastic strains, high strain rates and adiabatic heating.

By assuming isotropic material behaviour and von Mises plasticity, the engineering model proposed by Johnson and Cook [45] is adopted in the viscoplastic domain [44]. Thus, the equivalent stress σ_{eq} can be expressed as

$$\sigma_{eq} = [A + B p^n] [1 + C \ln \dot{p}^*] [1 - T^{*m}] \quad (4)$$

where A , B , C , n and m are material constants, p is the accumulated plastic strain, $\dot{p}^* = \dot{p}/\dot{p}_0$ is a dimensionless strain rate, \dot{p} is the plastic strain rate, \dot{p}_0 is a user defined reference strain rate, $T^* = (T - T_0)/(T_m - T_0)$ is the homologous temperature, T is the actual temperature, T_0 is the room temperature and T_m is the melting temperature. Since the strain rate and temperature effects on the flow stress are uncoupled, the Johnson–Cook model is easy to calibrate with a minimum of experimental data, and model constants can be found for several metals in the literature [5]. However, in contrast to the model, rate sensitivity is found experimentally to increase with increasing temperature, while the flow stress is decreasing [54]. Nevertheless, the model is generally accepted and has been implemented into several finite element codes.

To describe ductile fracture, Johnson and Cook also proposed a model including the effects of stress triaxiality, temperature, strain rate and strain path [43] on the failure strain. The model assumes that damage accumulates in the material element during plastic straining, and that the material breaks immediately when the damage reaches a critical value. In other words, the damage has no effect on the stress field as long as fracture has not taken place. Since it is known that damage degrades material strength during deformation, a coupled model is found necessary. Continuum damage mechanics [42], which is an attempt to treat ductile fracture quantitatively, may therefore be used to give a failure criterion. The main advantage of using this approach is that the damage model is coupled with the constitutive equation. In [42], the strain equivalence principle states that any constitutive equation for a damaged material can be derived in the same way as for the virgin material except that the usual stress is replaced by the effective stress. This implies that a unified model for damaged viscoplastic materials can be written as

$$\sigma_{eq} = (1 - D) [A + Br^n][1 + C \ln \dot{\epsilon}^*][1 - T^{*m}] \quad (5)$$

where D is the damage variable, defined in [42], and r is the damage accumulated plastic strain given as $\dot{r} = (1 - D)\dot{p}$. The damage variable takes values between 0 and 1, where $D = 0$ for an undamaged material and $D = 1$ for a fully broken material. However, the critical value of the damage variable, i.e. the value at which a macrocrack occurs, is less than 1. Hence, the failure criterion simply becomes

$$D = D_C \leq 1. \quad (6)$$

The evolution of damage is always related to irreversible strains, and may therefore be taken as a function of the accumulated plastic strain. Furthermore, experiments indicate that the damage remains equal to zero during the build-up of dislocations generating microcracks. Accordingly, it may exist a threshold of the accumulated plastic strain at which damage starts to evolve. Based on observations like these, a damage evolution rule is proposed as

$$\dot{D} = \begin{cases} 0 & \text{when } p < p_d \\ \frac{D_C}{p_f - p_d} \dot{p} & \text{when } p \geq p_d \end{cases} \quad (7)$$

where D_C is the critical damage, p_d is the damage threshold and p_f is a fracture strain depending on stress triaxiality, strain rate and temperature. Johnson and Cook [43] proposed an expression for the fracture strain as

$$p_f = [D_1 + D_2 \exp(D_3 \sigma^*)][1 + D_4 \ln \dot{p}^*][1 + D_5 T^*] \quad (8)$$

where D_1 – D_5 are material constants, $\sigma^* = \sigma_m/\sigma_{eq}$ is the stress triaxiality ratio, and σ_m is the mean stress.

The constitutive model defined by Eqs. (5)–(8) has been implemented in the explicit finite element code LS-DYNA [46] using a fully vectorized backward-Euler integration algorithm [44,47]. The model is applicable for shell and solid elements in three-dimensional analysis, as well as axisymmetric elements in two-dimensional analysis. In order to allow crack growth during penetration, the model was coupled with an element-kill algorithm available in the code. As the damage variable reaches its critical value D_C the damaged element is removed from the mesh.

The model describes linear elasticity, initial yielding, strain hardening, strain-rate hardening, damage evolution and fracture. For each of these phenomena one or several material parameters are required, and the total number of experimentally determined constants may seem considerable at first sight. However, all material constants can be identified from uniaxial tensile tests. In this study all targets are manufactured from Weldox 460 E, which is a thermo-mechanically rolled ferritic structural steel offering high strength combined with a high degree of ductility. Introductory quasi-static tensile tests at a strain rate of $5 \times 10^{-4} \text{ s}^{-1}$ were carried out to determine the elastic constants, and to study anisotropy and scatter in material properties as a function of plate thickness and batch number [48,49]. Tensile tests in three different directions (0° , 45° and 90°) with respect to the rolling direction of the material were conducted. Longitudinal and transverse strains were measured up to diffuse necking using two extensometers. The elastic properties, E and ν , are as given in Table 2. It was also found that the material could be characterised as isotropic both regarding stress and strain. However, it seems like damage after necking is directional and introduces anisotropy into the previously isotropic material (see also Fig. 13) at large plastic strains. The scatter of material properties between the different deliveries was found to be moderate. Nevertheless, it was decided that all material specimens should be manufactured from the same target plate, identical to the material used in the experimental penetration tests. Owing to the isotropic behaviour, only specimens parallel to the rolling direction have been tested.

All laboratory tests needed to calibrate the constitutive model are shown in Fig. 11. The data are obtained from (a) quasi-static smooth specimen tensile tests at large strains, (b) quasi-static notched specimen tensile tests with various notch radii, (c) tensile tests at various strain rates and (d) quasi-static tensile tests at various temperatures. The main features of the identification procedure are given below.

Fig. 11a shows the measured quasi-static true stress–strain curve for the target material all the way to fracture. The stress is based on continuous measurements of the applied load and the current area of the cylindrical specimen [50], while the strain is calculated as $\ln(A_0/A)$ where A_0 and A represent the initial and current area of the specimen, respectively. As seen, the target material is very ductile. Due to necking of the cylindrical specimens at large strains, there is a component of hydrostatic tension that tends to make the net tensile stress greater than the equivalent stress. According to Bridgman [51] and LeRoy et al. [52] the obtained stress in the smooth specimen should therefore be corrected. A comparison between the measured and the Bridgman–LeRoy corrected curve is shown in Fig. 11a. As seen, the correction is considerable at large strains, and the validity of the LeRoy empirical equation for this particular material is unknown. Therefore, only the yield stress constant A is determined from the smooth specimen tests.

In order to determine the strain hardening parameters B and n , and the critical damage parameter D_c , the cylindrical specimens with various notch radii as shown in Fig. 11b are used. Here, the damage evolution threshold p_a is chosen equal to zero. In a similar way as for the smooth specimen, the applied load and cross-sectional area in the notch are measured during testing. It is further assumed that the stress triaxiality ratio σ^* is approximately constant during plastic straining in each notched-specimen tensile test. The stress triaxiality ratio σ^* in the smooth specimen is on the other hand assumed to vary, and is therefore omitted in the calibration procedure. The different notches give a concentration of hydrostatic tension in the test specimen.

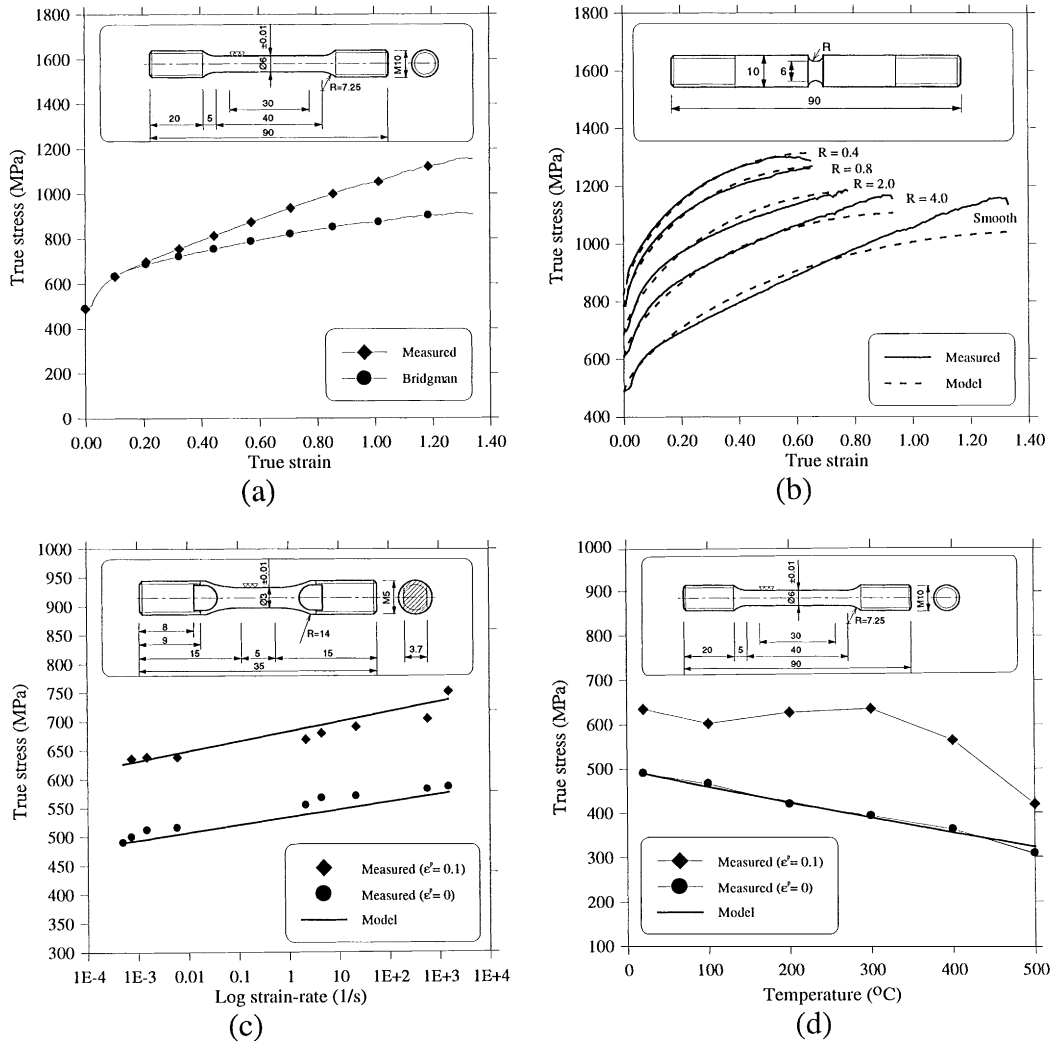


Fig. 11. Material test data used for identification of the model constants.

For a specified true strain, the stress is seen to increase when the notched radius R is reduced. It is also seen that the presence of hydrostatic tension significantly decreases the strain at which the material fractures. By taking the latter into account, the effect of hydrostatic tension on the failure strain is included in the model. The model constants B , n and D_c are determined from Eq. (5) when $\dot{p}^* = 1$, $T = T_0$ and σ^* is constant, which gives

$$\sigma_{eq} = \left(1 - \frac{D_c}{\bar{p}_f(\sigma_\alpha^*)} p_\alpha\right) (A + B r_\alpha^n) \tag{9}$$

where p_x , r_x and σ_x^* are discrete values of the variables p , r and σ^* , and \bar{p}_f is the measured fracture strain for the different notched specimens. The damage accumulated plastic strain r is calculated as

$$r = p - \frac{1}{2} \frac{D_c}{p_f(\sigma^*)} p^2 \quad (10)$$

for this particular case. The method of least squares is then used to minimise the difference between the experimental determined curves and the model by varying B , n and D_c simultaneously. The obtained material constants are given in Table 2, while Fig. 11b shows a comparison between the experimental curves and the model fit. As seen, good correlation is obtained for the notched specimens. However, the fit is somewhat poorer for the smooth specimen. This is probably caused by the variation in stress triaxiality during testing. The damage threshold p_d and the critical damage D_c can be identified from a tensile test where unloading is prescribed at equal intervals of strain in order to measure the variation of the modulus of elasticity, which may be used as a measure of damage [42]. Although this method is simple in principle, it is difficult to perform. Inverse modelling of the smooth and notched specimens using LS-DYNA will also be carried out in order to determine the damage parameters. The numerical approach, which is believed to give an accurate fit of the model to the measured data, should be used as a control of the simplified calibration procedure described above.

The viscous effect is obtained by means of uniaxial tensile tests at a range of different strain rates from 10^{-4} to 10^3 s^{-1} [53] as shown in Fig. 11c. From these tests an average effect of strain rate can be obtained. The figure shows that the strain rate sensitivity of the material is moderate and almost unaffected by the level of plastic strain. To have an average value of the strain rate sensitivity the data was fitted to the proposed model using the method of least squares for a plastic strain of $p = 0$ and $p = 0.1$ when $T = T_0$. The mean value of C is then used to describe the viscous effect. This is shown in Fig. 11c.

The effect of thermal softening on the true stress is shown in Fig. 11d. While the yield stress shows a linear decrease with increasing temperature, the ultimate tensile stress exhibits a local maximum at a temperature of about 300°C . This temperature region is known as the blue brittle region [40], and is caused by restraining of dislocations due to a release of second-order particles in carbon steels. By assuming adiabatic condition at high strain rates, the effect of thermal softening is included in the model by fitting the material constant m to the decreasing yield stress ($p = 0$, $\dot{p}^* = \dot{p}/\dot{p}_0 = 1$). A similar behaviour is seen at higher strains if the blue brittle effect is neglected. However, according to Harding [54] this uncoupling between thermal and viscous effects used in the Johnson–Cook model may not represent the correct physical behaviour observed in experiments.

The strain to fracture used in the damage evolution rule is given by Eq. (8). The expression in the first set of brackets gives the effect of hydrostatic stress on the strain to fracture for quasi-static conditions. This is shown in Fig. 12a, where the dimensionless triaxiality ratio in the centre of the specimen is calculated based on Bridgman's analysis as [55]

$$\sigma^* = \frac{1}{3} + \ln \left(\frac{a + 2R}{2R} \right) \quad (11)$$

where a and R are the initial radius of the specimen in the neck and the initial neck radius, respectively, since the triaxiality ratio is assumed constant during plastic straining. The strain to

failure is calculated as $\ln(A_0/A_f)$, where A_0 is the measured initial area of the specimen, and A_f is the measured area after fracture. All fracture areas have been measured in a light microscope, as seen in Fig. 13. The data point at $\sigma^* = 0$ was estimated based on a model proposed in [42]. The three material constants, D_1 , D_2 and D_3 , in the model have been fitted to the given data, and the curve has been extrapolated into the hydrostatic compression region as seen in Fig. 12a. The obtained values of D_1 – D_3 from the curve fit are as given in Table 2.

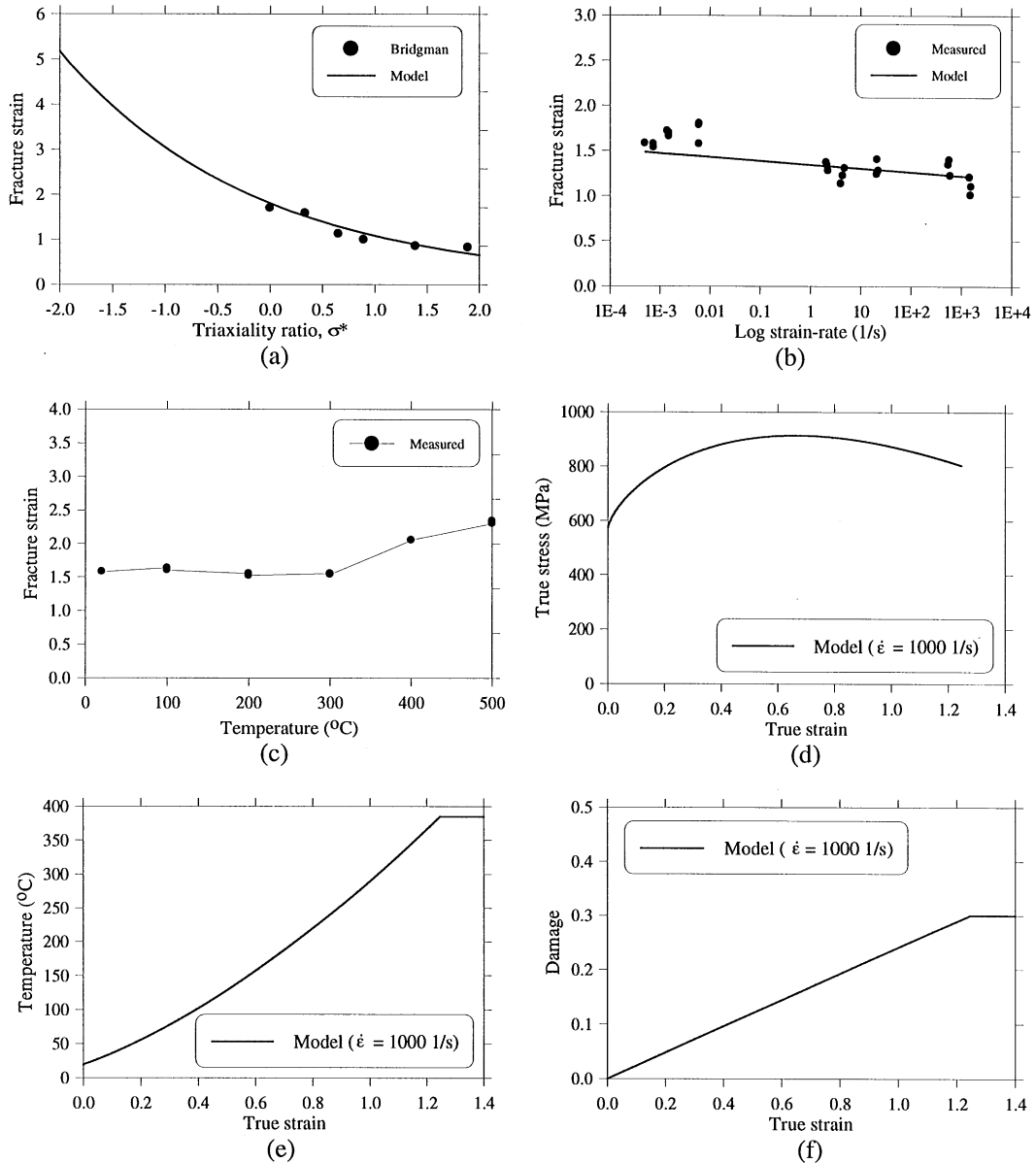


Fig. 12. Calibration of material model.

Table 2
Preliminary model constants for Weldox 460 E steel

Elastic constants and density			Yield stress and strain hardening			Strain rate hardening		Damage evolution	
E (GPa)	ν	ρ (kg/m ³)	A (MPa)	B (MPa)	n	\dot{p}_0, \dot{r}_0 (s ⁻¹)	C	D_c	p_d
200	0.33	7850	490	807	0.73	$5 \cdot 10^{-4}$	0.012	0.30	0

Adiabatic heating and temperature softening					Fracture strain constants				
C_p (J/kgK)	α	T_m (K)	T_0 (K)	m	D_1	D_2	D_3	D_4	D_5
452	0.9	1800	293	0.94	0.0705	1.732	-0.54	-0.0123	0

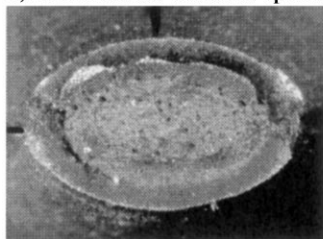
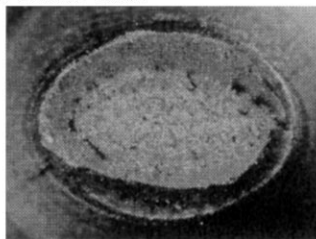
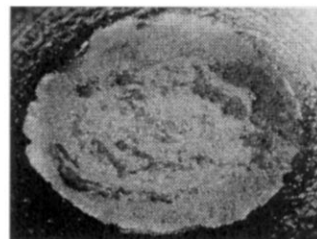
The effect of strain rate and temperature on the strain to failure is given in the second and third set of brackets in Eq. (8). The effect of strain rate is isolated from the temperature effect by considering the measured fracture strains for smooth specimens ($\sigma^* = 1/3$) at $T^* = 0$. This is shown in Fig. 12b, where the strain rate constant D_4 is fitted to the measured fracture strains. Both Fig. 12b and Fig. 13b indicate that the fracture strain decreases slightly with increasing strain rate. In a similar way, the effect of temperature on the fracture strain is isolated from the strain rate when $\dot{p}^* = \dot{p}/\dot{p}_0 = 1$, and the temperature constant D_5 is obtained from Fig. 12c. However, due to the blue brittle region the fracture strain is found to be unaffected by temperature up to 300–350°C. Therefore, D_5 is for this material chosen equal to zero.

As also indicated by Johnson and Cook [43], it appears that the fracture strain as a function of the triaxiality ratio shown in Fig. 12a is of primary importance. This is due to a rapid increase of the strain to fracture under hydrostatic compression. In most penetration problems a compression region will develop in front of the projectile at impact, and the damage evolution and fracture becomes strongly influenced by hydrostatic compression. As no material data is available in this region, the assumed function becomes critical and must be further investigated in coming work.

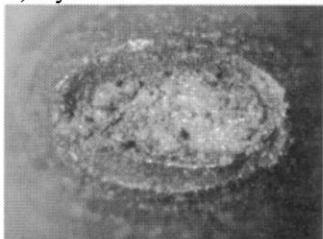
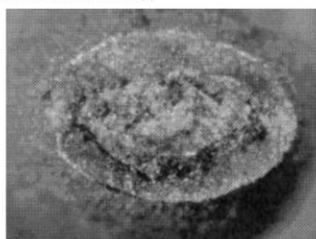
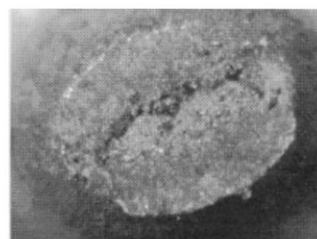
All material constants needed for the viscoplastic damage mechanics model are given in Table 2. The corresponding stress–strain relationship to fracture when $\sigma^* = 1/3$, obtained by using the constitutive model in Eq. (5), is shown in Fig. 12d. Here, adiabatic behaviour is assumed and the strain rate is chosen as $\dot{\epsilon} = 1000 \text{ s}^{-1}$. If this curve is compared to the quasi-static relationship given in Fig. 11a, the significance of adding several physical effects to the material behaviour during impact is shown. The adiabatic temperature rise during plastic deformation is seen in Fig. 12e. Both damage and temperature tends to soften the stress–strain curve. The damage evolution is shown in Fig. 12f. As seen, under the given conditions the damage develops linearly until the critical damage is reached.

The proposed model is used in the first approach of formulating a computational model of viscoplasticity and ductile damage for penetration problems. Therefore, both the model itself and

a) Smooth and notched specimen tensile tests:

Smooth, $\epsilon_f = 1.64$ R = 4.0, $\epsilon_f = 1.13$ R = 0.8, $\epsilon_f = 0.86$

b) Dynamic tensile tests at various strain-rates:

 $\dot{\epsilon} = 7.4 \cdot 10^{-4} \text{ s}^{-1}$, $\epsilon_f = 1.57$  $\dot{\epsilon} = 4.4 \text{ s}^{-1}$, $\epsilon_f = 1.22$  $\dot{\epsilon} = 1573 \text{ s}^{-1}$, $\epsilon_f = 1.11$

c) Tensile tests at various temperatures:

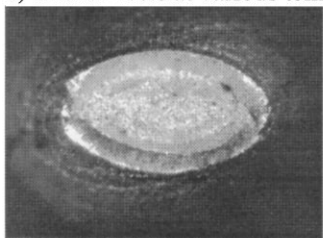
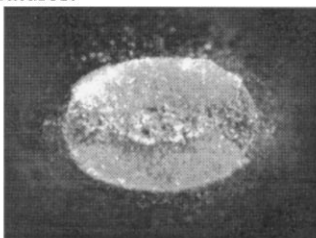
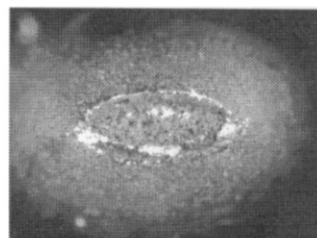
T = 100 °C, $\epsilon_f = 1.60$ T = 300 °C, $\epsilon_f = 1.54$ T = 500 °C, $\epsilon_f = 2.34$

Fig. 13. Fracture surfaces of some tensile test specimens as a function of (a) triaxiality, (b) strain rate and (c) temperature. Notice how the specimen geometry changes from isotropic to anisotropic behaviour with increasing strain to fracture.

the calibration procedures are under development. The main advantage of the model compared with most computational fracture models is that the damage evolution, giving material degradation, is fully coupled with the constitutive equation through the strain equivalence principle, i.e. the stress field depends on damage. Hence, damage contributes to the localisation of plastic deformation in the penetration process, and as the critical damage D_c is reached a macrocrack appears and fracture is assumed to occur. In the literature, the Johnson and Cook model has received some criticism. This is mainly due to the uncoupling between viscoplasticity and temperature. However, the model is here adopted as a first approach due to its relative simple formulation and calibration.

5. Numerical simulations

Preliminary numerical simulations of the penetration problem have been carried out to examine if the computational model of viscoplasticity and ductile damage [44] is able to predict the experimentally obtained target response during plugging. However, it is important to emphasize that some work still remains in order to draw final conclusions of the numerical results.

The axisymmetric finite element mesh used in the LS-DYNA [46] simulations is shown in Fig. 14. A total of 3550 4-node axisymmetric elements with one-point integration were applied in the model, giving 25 elements through the plate thickness. The required CPU time varied between 5–9 h per run on a HP 715/100 workstation. Due to the CPU requirement, the analyses were stopped before the elastic rebound of the target plate was completed. Therefore, the final target deformation is not obtained.

The target material was modelled as elastic-viscoplastic coupled with ductile damage, using Eqs. (5)–(8) and the material constants given in Table 2. The projectile of hardened tool steel was modelled as linear elastic with Young's modulus $E_p = 200,000$ MPa and Poisson's ratio $\nu_p = 0.33$ due to the lack of reliable projectile material data. At impact velocities near the ballistic limit this assumption seems to be sufficient. However, at higher impact velocities the projectile mushrooming may become considerable. Projectile material data will be included in the next version of the numerical model.

In the simulations, the plate was fully clamped at the support, while the projectile was given an initial velocity v_i as defined in Table 3. The contact between the projectile and target was modelled using a penalty formulation without friction. The effect of friction will be investigated in future work. No attempt has so far been made in order to reveal the possible mesh dependence of the solution. However, according to Needleman [56], pathological mesh size effects do not occur in finite element simulations involving material softening due to e.g. damage if the strain rate dependence of the material is accounted for. More severe numerical difficulties are associated with the dynamic localisation problem, and a lot of elements are required over the target thickness. An adaptive solution method under development will be tested in later simulations in order to resolve the narrow shear bands.

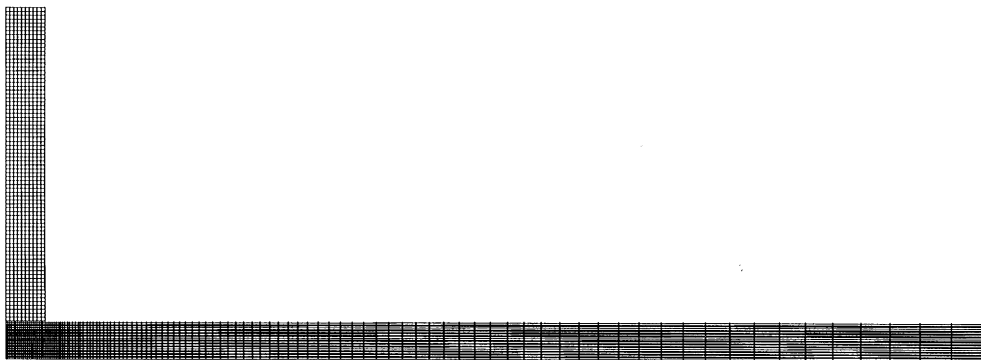


Fig. 14. Finite element model of the penetration problem.

Table 3
Numerical programme and results

Run #	Input data			Experimental		Numerical	
	v_i (m/s)	m_p (g)	h_t (mm)	v_r (m/s)	v_{rpl} (m/s)	v_r (m/s)	v_{rpl} (m/s)
10-9	296.0	196.7	9.7	218	243	224	232
12-15	189.6	196.7	12.1	42	62	0	0
12-1	303.5	196.6	12.1	200	242	206	265
12-2	244.2	196.9	12.1	133	188	109	142
12-9	224.7	196.9	12.0	114	169	94	123
12-4	200.4	197.0	12.0	71	104	0	0
12-8	181.5	196.7	12.1	0	0	0	0
12-N1	215.0	197.0	12.0	–	–	69	76
12-N2	210.0	197.0	12.0	–	–	38	47
12-N3	205.0	197.0	12.0	–	–	0	0

The scope of the simulations was to examine run # 10-9 and run # 12-15 in detail regarding a direct comparison with the experimental observations given in Figs. 8–10, and to construct the ballistic limit curve for the 12 mm thick Weldox 460 E steel target based on the numerical results. Table 3 gives the numerical test programme, together with the major response parameter, which is defined as the residual velocity of the projectile and plug. The agreement between the experimentally and numerically obtained velocities is excellent at the highest velocities. However, in the simulation of test # 12-15 perforation was not obtained. In order to define the ballistic limit velocity, run # 12-N1 to 12-N3 were conducted. From these simulations, the ballistic limit velocity was found from run # 12-N3 to be 205 m/s. This gives a deviation from the experimentally obtained ballistic limit of 10%, which is acceptable concerning the complexity of the problem. Based on the results, it was decided to compare test # 12-15 with the numerical results of run # 12-N2, since the initial velocity in both cases is approximately 5 m/s above the respective ballistic limit.

Plots of the deformed element mesh during perforation of run # 10-9 and 12-N2 are shown in Figs. 15 and 16, respectively. If the results are compared with Figs. 8 and 9, where the high-speed camera images from the experiments are shown, excellent agreement is found between the numerical simulations and the experimental observations. In the first phase, the projectile indents the target. During this short period of time, the target mass in front of the projectile is accelerated, and the deformation mechanism changes into a highly localised shear zone surrounding the projectile nose. Damage develops rapidly in the shear zone due to the severe plastic straining of the elements closest to the projectile–target interface. The critical damage is reached, the elements start to erode, and the crack propagates towards the rear side of the target. In the final stage, the failure mode is combined shear and tensile failure, as also obtained during testing. The bulge is highly localised, with hardly any global target deformation in run # 10-9. In run # 12-N2, where the initial velocity is close to the ballistic limit, the perforation process slows down and a larger part of the plate is activated. This involves a larger global target deformation, as

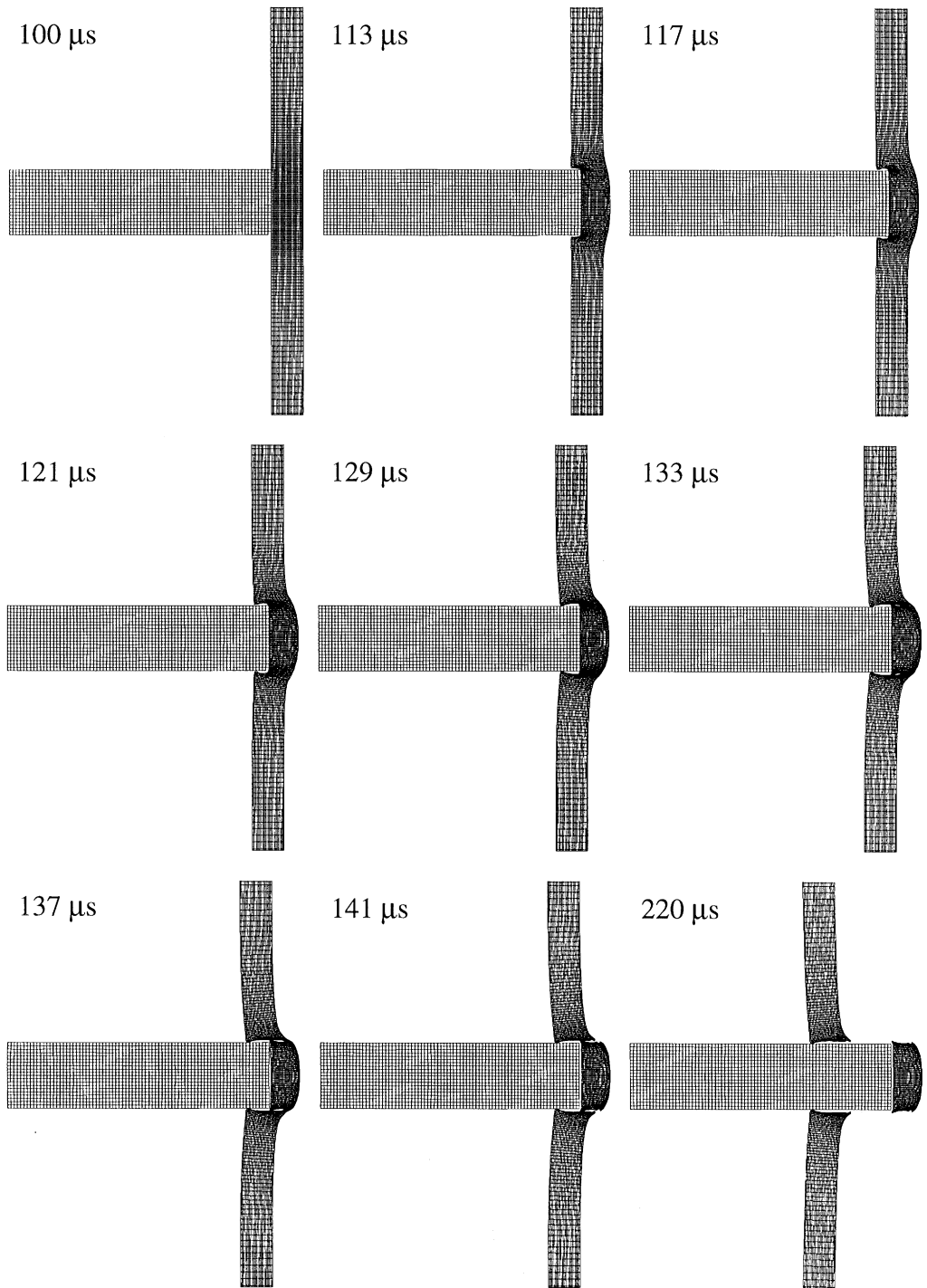


Fig. 15. Plots of deformed mesh during perforation from run # 10-9.

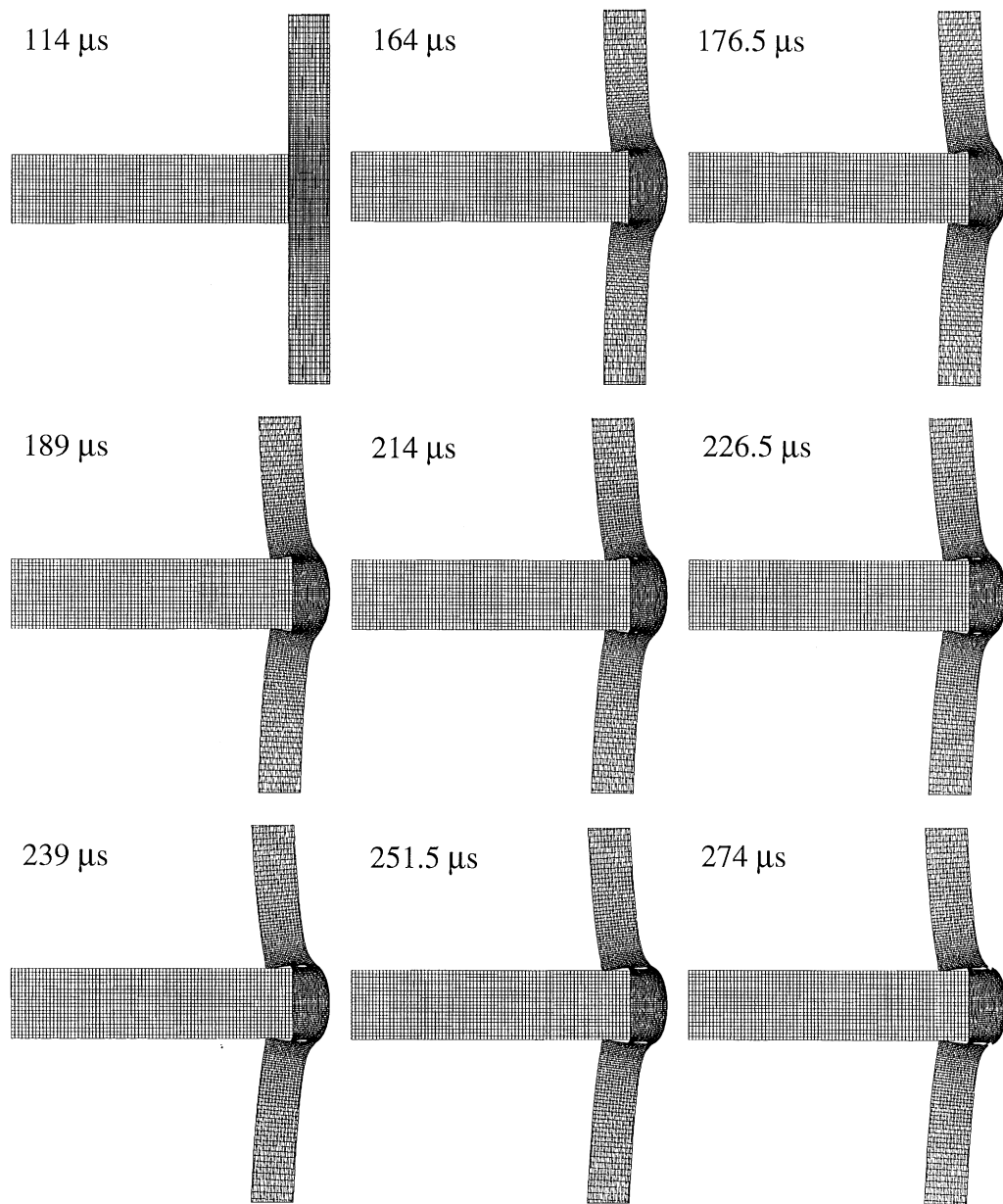


Fig. 16. Plots of deformed mesh during perforation from run # 12-2N.

also seen in Fig. 4c. The plug is fully fractured before complete separation from the target occurs, and the plug shape seems to be very close to the experimental one (Fig. 6). The typical target lip due to tensile straining at the rear side (Fig. 5) is described. No frontal bulge is obtained in any of the simulations.

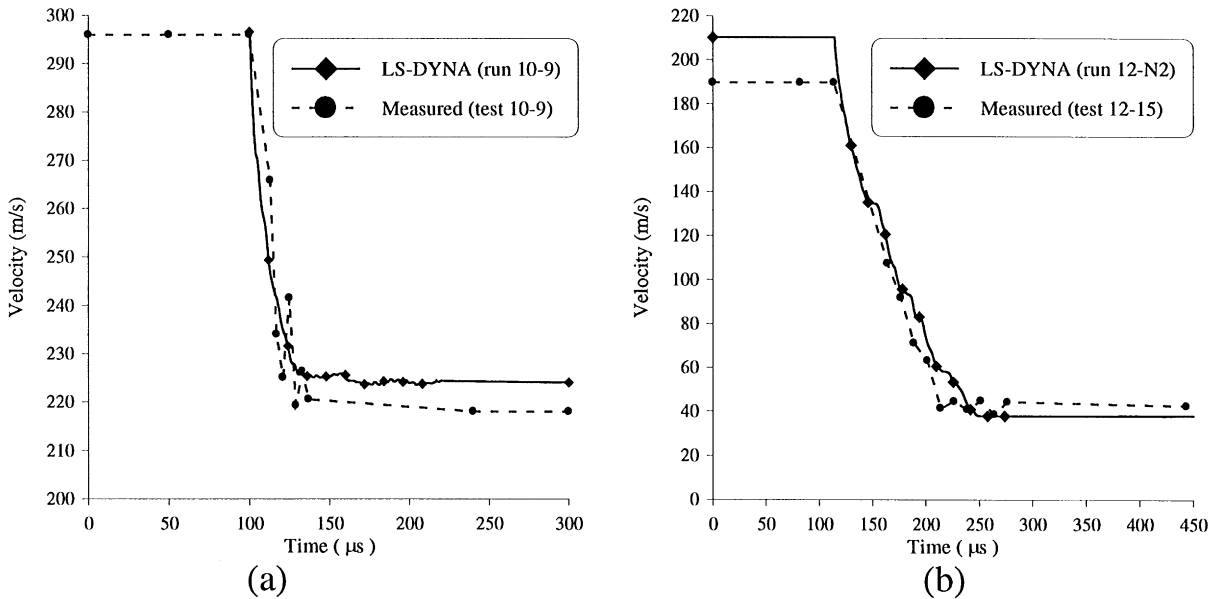


Fig. 17. Numerical vs. experimental velocity–time curves for (a) test and run # 10-9 and (b) test # 12-15 and run # 12-N2.

The projectile velocity–time curves from the numerical simulations of run # 10-9 and 12-2N have been compared with the high-speed camera measurements of test # 10-9 and 12-15 in Fig. 10. This is shown in Fig. 17. Not only are the residual velocities of the projectile closely described, but also the slope of the curves and the perforation times seem to coincide. From the simulations, it seems like the projectile impacts the plug several times during penetration. At impact, the plug mass is accelerated by stress waves to a higher velocity than that of the projectile. However, due to restraining by the shear zone, the plug is prevented from leaving the target. The projectile catches up with the plug, giving it a new impact, and contact between the bodies are lost once more. At or very close to fracture, this impact becomes a collision between two free bodies, and the plug leaves the target at a higher velocity. This may explain the observed difference in projectile and plug residual velocity, and the measured fluctuations in the velocity–time curves close to fracture. A comparison between the measured and simulated projectile residual velocities given in Table 3 for the 12 mm thick steel target is shown in Fig. 18. Due to the disagreement in the ballistic limit velocity of 10%, the data does not coincide except for the highest impact velocities. In Fig. 18, also the model of Recht and Ipson [35] has been plotted for the obtained ballistic limits of 185 and 205 m/s, respectively. As seen, the model gives a close representation of the numerical results.

The simulations indicate that the maximum strain rate in the shear zone is nearly $200,000 \text{ s}^{-1}$ for run # 10-9, and $100,000 \text{ s}^{-1}$ for run # 12-2N. The calculated temperature increase due to adiabatic heating is about 350°C in both runs. Also the energy absorption in the different materials has been calculated, and it is found that most of the work is carried out in global target deformation. However, since the projectile is modelled as an elastic material, the calculated energy distribution becomes inaccurate.

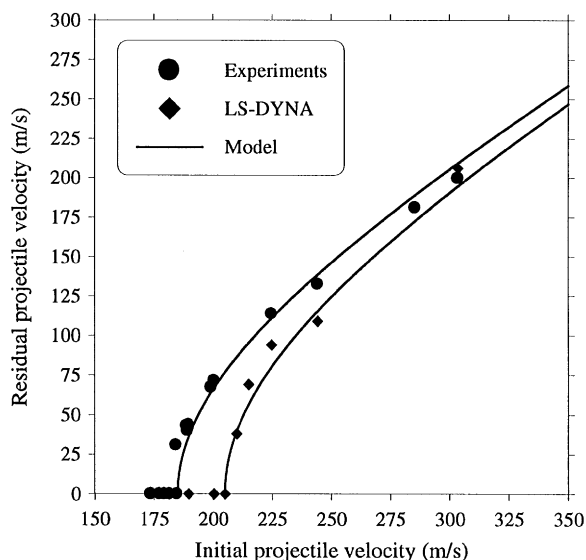


Fig. 18. Comparison between calculated and measured ballistic limit curves.

From the preliminary simulations the numerical model seems to capture the main target response during the penetration process, and promising results are obtained. However, to exactly determine the ballistic limit velocity in the penetration problem using numerical simulations is still a challenge. This is in any case the parameter of primary interest in design. Nevertheless, the ballistic limit velocity obtained in the numerical study is within the expected accuracy for such complex problems. In coming work the sensitivity of the numerically determined ballistic limit velocity to variations in the material constants will be studied. The effect of changing model parameters, such as target thickness and projectile nose shape will be investigated both experimentally and numerically.

6. Summary and conclusions

This paper presents a research programme in progress where the main objective is to study the behaviour of steel plates impacted by blunt-nosed cylindrical projectiles in the lower ordnance velocity regime.

A compressed gas gun capable of launching a 250 g sabot mounted projectile to a maximum velocity of 1000 m/s has been built during the study. The gas gun is used to obtain high-precision penetration test data for verification of solution methods. During testing, the main instrumentation is provided by a digital high-speed camera system. In addition to visualisation of the impact process, the digital images are used to obtain travelled distance, velocity and acceleration for the assumed rigid bodies as a function of penetration time.

In this paper, emphasis has been on an experimental programme carried out to determine the ballistic limit curve of a 12 mm thick Weldox 460 E steel plate. Some of the most important experimental findings are reported and discussed, and two typical perforation tests are presented in detail. All targets failed by shear plugging. A metallurgical examination of the penetrated target plates is also presented. This has revealed void growth in the localised shear zone, indicating a ductile fracture.

To be able to predict the different phenomena taking place during penetration, characterisation of the target material under impact generated high strain rate loading conditions has been found necessary. This involves not only the stress–strain response for large strains, high strain rates and temperatures, but also the accumulation of damage and the mode of failure. A coupled constitutive model of viscoplasticity and ductile damage was used in order to calculate projectile penetration and failure. The model, which has been implemented into the finite element code LS-DYNA, has been coupled with an element-kill algorithm available in the code that removes the damaged element from the model when the damage variable reaches its critical value.

Even if the total number of material constants required in the model seems considerable at first sight, they can readily be identified from quasi-static and dynamic tensile tests. All laboratory test data needed to calibrate the model is presented and discussed, and the model constants for Weldox 460 E steel are given in tabular form.

Preliminary numerical simulations of the plate penetration problem have been carried out giving promising results, and it seems like the numerical model is capable of describing the main target response and physical behaviour observed during perforation. However, the numerical solution overpredicts the ballistic limit velocity by approximately 10%. At higher velocities, good agreement between the numerical model and experimental results is obtained.

In coming work, the sensitivity of the numerical model to variations in material constants and mesh size will be studied. Also the effect of changing model parameters, such as target thickness and projectile nose shape, will be investigated both experimentally and numerically. In addition, an adaptive solution procedure will be tested in order to resolve the high strain gradients in the plate penetration problem.

Acknowledgements

The authors would like to thank the Norwegian Defence Construction Service for their financial support of the research project that forms the basis of the present work. Furthermore, the authors would like to express their gratitude to Mr. Knut Holen for considerable assistance in establishing the high-speed camera measurement techniques and to Dr. Torodd Berstad for model implementation and help in obtaining the numerical results. Finally, Mr. Arnfinn Jenssen is also gratefully acknowledged for his help during the project.

References

- [1] Backman ME, Goldsmith W. The mechanics of penetration of projectiles into targets. *Int J Engng Sci* 1978;16:1–99.
- [2] Corbett GG, Reid SR, Johnson W. Impact loading of plates and shells by free-flying projectile. *Int J Impact Engng* 1996;18(2):141–230.

- [3] Anderson Jr CE, Bodner SR. Ballistic impact: the status of analytical and numerical modeling. *Int J Impact Engng* 1988;7(1):9–35.
- [4] Zukas JA et al. *Impact dynamics*. Florida: Krieger, 1992.
- [5] Zukas JA, et al. *High velocity impact dynamics*. New York: Wiley, 1990.
- [6] Brown SJ. Energy release protection for pressurized systems – review of studies into impact/terminal ballistics. *Appl Mech Rev* 1986;39:177–201.
- [7] Jonas GH, Zukas JA. Mechanics of penetration: analysis and experiment. *Int J Engng Sci* 1978;16:879–903.
- [8] Corran RSJ, Shadbolt PJ, Ruiz C. Impact Loading of plates – an experimental investigation. *Int J Impact Engng* 1983;1(1):3–22.
- [9] Awerbuch J, Bodner SR. Experimental investigation of normal perforation of projectiles in metallic plates. *Int J Solids Struct* 1974;10(6):685–99.
- [10] Hanchak SJ, Altman BS, Forrestal MJ. Perforation of HY-100 steel plates with long rod projectiles. *Proceedings of 13th Army Symposium on Solid Mechanics*, 17–19 August, Plymouth, Massachusetts, 1993.
- [11] Piekutowski AJ, Forrestal MJ, Poormon KL, Warren TL. Perforation of aluminium plates with ogive-nose steel rods at normal and oblique impact. *Int J Impact Engng* 1996;18(7–8):877–87.
- [12] Liss J, Goldsmith W. Plate perforation and phenomena due to normal impact by blunt cylinders. *Int J Impact Engng* 1984;2(1):37–64.
- [13] Goldsmith W, Finnegan SA. Penetration and perforation processes in metal targets at and above ballistic velocities. *Int J Mech Sci* 1971;13:843–66.
- [14] Lethaby JW, Skidmore IC. The deformation and plugging of thin plates by projectile impact. *Mech Prop of Materials at High Rates of Strain*, Conference Series No. 21, Oxford, 1974;429–41.
- [15] Woodward RL, De Morton ME. Penetration of targets by flat-ended projectiles. *Int J Mech Sci* 1976;18:119–27.
- [16] Shadbolt PJ, Corran RS, Ruiz C. A comparison of plate perforation models in the sub-ordnance velocity range. *Int J Impact Engng* 1983;1(1):23–49.
- [17] Awerbuch JA, Bodner SR. Analysis of the mechanics of perforation of projectiles in metallic plates. *Int J Solids Struct* 1974;10:671–84.
- [18] Langseth M, Larsen PK. The behaviour of square steel plates subjected to a circular blunt ended load. *Int J Impact Engng* 1992;12(4):617–38.
- [19] Marom I, Bodner SR. Projectile perforation of multi-layered beams. *Int J Mech Sci* 1979;21:489–504.
- [20] Wierzbicki T, Hoo Fatt MS. Deformation perforation of a circular membrane due to rigid projectile impact. *AMD-vol. 127/PVP-vol. 225, Dynamic Response of Structures to High-Energy Excitation*, ASME, 1991.
- [21] Ravid M, Bodner SR. Dynamic perforation of viscoplastic plates by rigid projectiles. *Int J Engng Sci* 1983;21(6):577–91.
- [22] Liu J, Jones N. Shear and bending response of a rigid plastic circular plate struck by a mass. *Mech Struct Mach* 1996;24(3):361–88.
- [23] Liss J, Goldsmith W, Kelly JM. A phenomenological penetration model of plates. *Int J Impact Engng* 1983;1(4):321–41.
- [24] Belytschko T, Lin JJ. A three-dimensional impact-penetration algorithm with erosion. *Comput Struct* 1987;25(1):95–104.
- [25] Sewell DA, Ong ACJ, Hallquist JO. Penetration calculations using an erosion algorithm in Dyna. *Proceedings of 12th International Symposium on Ballistics*, San Antonio, USA, 1990; 208–17.
- [26] Schwer LE, Day J. Computational techniques for penetration of concrete and steel targets by oblique impact of deformable projectiles. *Nucl Engng Des* 1991;125:215–38.
- [27] Chen EP. Numerical simulation of shear induced plugging in HY100 steel plates. *Int J Damage Mech* 1992;1:132–43.
- [28] Belytschko T. On difficulty levels in non linear finite element analysis of solids. *Bull Int Assoc Comput Mech* 1996;2(2):6–8.
- [29] Børvik T, Langseth M, Malo KA. A compressed gas gun for impact testing. *Fortifikatorisk Notat No. 242/97*, Norwegian Defence Construction Service, 1997.
- [30] Børvik T, Vestli K, Langseth M. Determination of projectile path during ballistic penetration by use of a high-speed digital camera. *Association of High-Speed Photography Conference*, Cambridge, UK, April 1997.

- [31] Børvik T, Holen K, Langseth M, Malo KA. An experimental set-up used in ballistic penetration. Proceedings of Fifth International Symposium on Structures under Shock and Impact, Thessaloniki, Greece, 24–26 June 1998;683–92.
- [32] Børvik T, Langseth M, Malo KA, Hopperstad OS. Experimental determination of the ballistic limit in weldox 460 E steel plates. Proceedings of 11th International Conference on Experimental Mechanics, Oxford, U.K., 24–28 August 1998;233–8.
- [33] Goldsmith W, Tham E, Tomer D. Yawing impact on thin plates by blunt projectiles. *Int J Impact Engng* 1995;16(3):479–98.
- [34] Forrestal MJ, Hanchak SJ. Perforation of HY-100 steel plates with 4340 R_c 38 and T-250 maraging steel rod projectiles. Proceedings of International Symposium on Transient Loading and Response of Structures (honouring Mr. Arnfinn Jønsen), Trondheim, Norway, 25–27 May 1998.
- [35] Recht RF, Ipson TW. Ballistic perforation dynamics. *Int J Appl Mech (Trans ASME)* 1963;30:384–90.
- [36] Aune A, Børvik T, Langseth M. Quasi-static point-loaded weldox 460 E steel plates (in Norwegian). Fortifikatorisk Notat No. 241/96, Norwegian Defence Construction Service, 1996.
- [37] Hawkyard JB, Eaton D, Johnson W. The mean dynamic yield strength of copper and low carbon steel at elevated temperatures from measurements of the “mushrooming” of flat-ended projectiles. *J Mech Sci* 1968;10:929–48.
- [38] Lindholm US, Johnson GR. Strain rate effects in metals at large shear strains. Proceedings of the 29th Sagamore Army Materials Conference entitled Material Behaviour Under High Stress and Ultrahigh Loading Rates, New York, 1982.
- [39] Børvik T, Leinum JR, Solberg JK, Hopperstad OS, Langseth M. Microscopic examination of steel plates penetrated by blunt-nosed projectiles. 1999, in preparation.
- [40] Dieter GE. *Mechanical metallurgy*. London: McGraw-Hill, 1988.
- [41] Lemaitre J, Chaboche J-L. *Mechanics of solid materials*. Cambridge: Cambridge University Press, 1990.
- [42] Lemaitre J. *A Course on damage mechanics*. Berlin: Springer, 1992.
- [43] Johnson GR, Cook WH. Fracture characteristics of three metals subjected to various strains, strain rates, temperatures, and pressures. *Engng Fracture Mech* 1985;21:31–48.
- [44] Hopperstad OS, Berstad T, Børvik T, Langseth M. Computational model for viscoplasticity and ductile damage. Proceedings of fifth International LS-DYNA User Conference, Michigan, USA, 21–22 September 1998.
- [45] Johnson GR, Cook WH. A constitutive model and data for metals subjected to large strains, high strain rates and high temperatures. Proceedings of Seventh International Symposium on Ballistics, The Hague, The Netherlands, April 1983.
- [46] Hallquist JO, Stillman DW, Lin T-L. *LS-DYNA3D user’s manuals*. Livermore Software Technology Corporation, Report 1007, Rev 2, 1994.
- [47] Berstad T, Hopperstad OS, Langseth M. Elasto-viscoplastic constitutive models in the explicit finite element code LS-DYNA3D. Proceedings of second International LS-DYNA3D User Conference, San Francisco, September 20–21, 1994.
- [48] Børvik T, Aune A, Hopperstad OS, Langseth M. Quasi-static tensile tests of weldox 460 E steel plates – introductory study. Fortifikatorisk Notat No. 250/97, Norwegian Defence Construction Service, 1997.
- [49] Børvik T, Aune A, Hopperstad OS, Langseth M. Quasi-static tensile tests of weldox 460 E steel plates – variation of material properties. Fortifikatorisk Notat No. 255/97, Norwegian Defence Construction Service, 1998.
- [50] Søvik OP. Numerical modelling of ductile fracture – a damage mechanics approach. Dr Ing Thesis, Department of Machine Design and Materials Technology, NTNU, 1996.
- [51] Bridgman PW. *Studies in large plastic flow fracture*. Cambridge, MA: Harvard Univ Press, 1964.
- [52] LeRoy G, Edwards G, Ashby MF. A model of ductile fracture based on the nucleation and growth of voids. *Acta Metal* 1981;29:1509–22.
- [53] Quick M, Del Grande A, Spinelli R, Albertini C, Børvik T, Hopperstad OS, Langseth M. Tensile tests at low, medium and high strain rate of weldox 460 E. Fortifikatorisk Notat No. 251/97, Norwegian Defence Construction Service, 1997.

- [54] Harding J. The development of constitutive relationships for material behaviour at high rates of strain, Inst Phys Conf Ser No. 102: Session 5, Oxford, UK, 1989.
- [55] Hill R. The mathematical theory of plasticity. Oxford: Oxford University Press, 1950.
- [56] Needleman A. Material rate dependence and mesh sensitivity in localization problems. *Comput Methods Appl Mech Engng* 1988;67:69–85.